Photo-electrochemical and enhanced photocatalytic activity of CdS/rGO nanocomposites prepared by hydrothermal method

Chao Li[1,2], Zhiqiang Wei[1,2,*] (iD), Yuanrui Chen[1,2], Long Ma[1,2], Shangpan Huang[1,2], Ling Li[1,2], and Jinhuan Ma[1,2]

[1] *School of Science, Lanzhou University of Technology, Lanzhou 730050, China*
[2] *State Key Laboratory of Advanced Processing and Recycling of Non-Ferrous Metals, Lanzhou University of Technology, Lanzhou 730050, China*

ABSTRACT

CdS/rGO nanocomposites with different mass ratio of rGO were fabricated via a facile one-pot hydrothermal method. The influences of different ratios on the microstructure, photo-electrochemical, and photocatalytic properties of the as-prepared samples were investigated. The experimental results show that CdS/rGO nanocomposites are hexagonal structure, one-dimensional CdS nanorods decorated on the surface of graphene. CdS/rGO nanocomposites show excellent visible light absorption and the band gap smaller than that of pure CdS and occur red shift. The photoluminescence spectra, transient photocurrent response and electrochemical impedance spectra indicate this nanostructure can accelerate the separation and migration efficiency of photogenerated electron–hole pairs, inhibit the recombination of photogenerated carries and and enhance electron transportation in the photocatalytic reactions. CdS/rGO nanocomposites display enhanced photocatalytic activity in degradation of MO under the simulated sunlight irradiation than that of pure CdS. In addition, in the photocatalytic degradation process $\cdot O_2^-$ and $\cdot OH$ play the key role.

1 Introduction

In recent decades, A particularly serious water pollution problem in the world due to the continuous improvement of people's living standard and the rapid industrial development [1–3]. Among them, organic dye wastewaters possess biological toxicity, high concentration and chroma, it is degrade under natural surroundings with difficulty, and brings great harm to human survival and ecological balance [4, 5].Various treatment technologies have been expanded to remove pollutants, such as chemical oxidation, adsorption, flocculation precipitation, microbial decomposition, ozone oxidation and photocatalytic degradation, et al. [6–8]. Photocatalytic technology is considered to have unlimited prospects

Address correspondence to E-mail: qianweizuo@163.com

in the degradation of harmful water pollutants due to its highly active, cheap cost and environmental friendliness. Especially the degradation of organic compounds into non-toxic products under mild reaction conditions without additional additives and equipment [9, 10].

There are many methods for preparing and synthesizing photocatalysts, such as hydrothermal, solvothermal, sol–gel, chemical precipitation, and microwave. This paper adopts the hydrothermal method because of its simple operation, satisfactory crystallinity, high purity, low water pollution and low cost, and it can be used for large-scale production. However, the hydrothermal method is carried out in a reactor, and the crystallization process cannot be directly observed, and its morphology cannot be precisely controlled [11–13].

CdS is an ideal semiconductor photocatalys with narrow band gap (2.42 eV) and good visible light response, the absorption spectrum is very close to the solar spectrum [14–16]. It is widely used in field-effect transistors, solar cells, photosensitive sensors, nonlinear optical materials and photocatalysis [17–20]. However, the high recombination rates of photogenerated electron–hole pairs leads to inefficient photocatalytic activity, and the photocorrosion problem obstruct its industrial application. Therefore, it is essential to enhance its photocatalytic performance by doping, compounding, precious metal deposition and other surface modification method [21–23]. rGO possess unique two-dimensional hexagonal honeycomb lattice structure of sp2-hybridized carbon atoms with greatly specific surface area, outstanding conductive properties and high electron mobility [24–26]. rGO as a catalyst support combined with semiconductors can promote the abruption of photogenerated carriers, suppress the recombination of photogenerated carriers and enhance its photocatalytic performance and stability [27–31]. Ma et al. [32] used a new synthesis strategy to develop high graphene oxide-CdS quantum dot nanocomposites, found rGO layers play a significant role due to availably prevent the regroup of photogenerated carrier pairs. Singh et al. [33] synthesized an active CdS/rGO photocatalyst through a high-temperature gas–solid reaction. The study of hydrogen production by water splitting found that the high electron mobility of rGO resulted in more robust photocatalytic performance. Ranjan et al. [34] reported that CdS supported electrochemically reduced rGO for photoreduction of water to hydrogen and found that heterojunction formation is the key to a better activity hydrogen formation from photochemical reducing water.

In this work, CdS/rGO nano-semiconductor composites with different mass specific values of rGO were successfully manufactured through a handy one-step hydrothermal method by controlling the quality of the GO compound. And microstructure, photo-electrochemical and photocatalytic characterization of the samples by X-ray diffraction (XRD), high-resolution transmission electron microscopy (HRTEM), X-ray energy dispersive spectroscopy (XEDS), X-ray photoelectron spectrometer (XPS). and N2 adsorption–desorption technique, photoluminescence spectroscopy (PL) and UV–vis diffuse reflection spectrum. Electrochemical impedance spectra (EIS) and transient photocurrent response were tested to estimate photo-generated charge recombination and electron convey ability. The effects of the composite ratio estimate the photocatalytic performance of samples by starting now methods simulating the photodegradation of samples added to an aqueous solution containing methyl orange (MO) under sunlight. The mechanism of enhancing visible light catalytic activity was proposed. As far as we know, there are some reports on the photocatalytic performance of CdS/rGO nano-semiconductor composites in the literature. We base our research on the effects of different composite ratios on the microstructure, optical properties, photoelectrochemical and photocatalytic properties. In addition, the composite catalyst showed better photocatalytic activity than the original CdS. A possible mechanism for enhancing the photocatalytic performance of CdS/rGO nano-semiconductor composites is also proposed.

2 Experimental

2.1 composites of CdS/rGO nanocomposites

CdS/rGO nanocomposites with diverse proportions of rGO (0–2.5%) were prepared via one-step hydrothermal method. The typical synthesis process of CdS/rGO nanocomposites is as follows: Similar to our previous report, graphene oxide (GO) is made by oxidation of graphite flakes using a modified

Hummers method [25]. According to the molar ratio of cadmium source and sulfur source at 1:6, weighed 0.0025 mol Cd $(CH_3CO_2)_2$ and 0.015 mol CH_4N_2S used as precursors, then dissolved in 40 mL deionized water and 40 ml ethylenediamine to obtain a mixed solution. Meanwhile, a certain amount of graphene oxide is weighed in the above mixed solution. The resultant mixture was firstly ultrasonic treatment for 30 min, then magnetic stirred for 30 min to mix completely. Subsequently, the obtained transferred the mixed solution to a 100 mL stainless steel autoclave lined with polytetrafluoroethylene. Keep the sealed autoclave at 185 °C under the hydrothermal strip for 12 h. After the reaction was completed, the autoclave was naturally cool down to room temperature. Centrifuge the solution and wash 3 times alternately with absolute ethanol and deionized water, dry under vacuum at 60 °C for 12 h to obtain CdS/rGO samples. CdS/rGO composites with different GO mass ratio of 0.5%, 1%, 1.5% and 2.5% were prepared the sample following the same steps as above, and the samples were denoted as recorded as: GCS-0.5, GCS-1.0, GCS-1.5 and GCS-2.5, respectively.

2.2 Characterization

The crystalline powder product was recorded on an X-ray diffractometer (Rigaku, Japan, D/Max-2400), and recorded with Cu Kα radiation (λ = 0.15406 nm) at 40 kV and 80 mA, scanning rate 0.2°/s and step size 0.02°. Scanning electron microscope (SEM, JEOL JSM-6701F) and high-resolution transmission electron microscopy (HRTEM, JEM-2010) were performed to observe the morphology and microstructure of the samples. The chemical composition of the product is measured by X-ray energy dispersive spectroscopy (XEDS). The surface chemical composition and chemical state of elements were studied by X-ray photoelectron spectrometer (XPS, PHI-5702). The specific surface area and pore parameters were measured by nitrogen adsorption–desorption analyzer Micromeritics, ASAP2020. Ultraviolet–visible (UV–Vis) spectrophotometer (PERSEE TU-1901) was performed to characterize the samples' optical absorption and bandgap energy. The photoluminescence (PL) spectra were recorded by luminescence spectrophotometer (LS-55).

2.3 Photo-electrochemical measurement

Electrochemical impedance spectra (EIS), Mott-Schottky curves and transient photocurrent response were Tested using an electrochemical workstation (CS350, Wuhan CorrTest, China) with a standard three-electrode battery cell in Na_2SO_4 (0.1 M) electrolyte. Prepare working electrode by dropping CdS/rGO samples onto the surface of the Indium Tin Oxide (ITO) conductive glass, the reference electrode is a saturated calomel electrode (SCE), and the counter electrode is a Platinum foil. The photocurrent-time (I-t) curves were obtained under fixed bias potential of 0.5 V. The EIS Nyquist plot was recorded in the frequency extent of 0.01 Hz to 100 kHz with a vibration amplitude of 5 mV, and a 500 W xenon lamp was used as the aroused light source.

2.4 Photocatalytic experiment

The photocatalytic activity of CdS/rGO nano-scale semiconductor materials was evaluated in VS-GCH-XE-300 photochemical reaction apparatus. In the experiment, methyl orange (MO) solutions were used to simulate dye wastewater, and 500 W xenon lamp was used to simulate visible light for degradation within 120 min at room temperature. In the degradation experiment, a certain amount of samples were scattered in 100 ml MO solution (20 mg/L). The photocatalytic efficiency was defined as $(C_0 - C_t)/C_0 \times 100\%$, where C_0 and C_t stand for the initial concentration of MO solution and the concentration of dye after 30 min illumination, respectively. Meanwhile, sonicated the suspension for 30 min in the dark before illumination to striked a balance between adsorption and desorption. Subsequently, the photocatalytic degradation reaction was in progress for 150 min under the irradiation of a 300 W xenon lamp. After a certain time interval (30 min), 3 mL of the reaction solution was taken out. The concentration of the MO dye was determined by measuring the absorbance of the solution using a UV–vis spectrophotometer. And then collect the dispersed photocatalyst after the photocatalytic reaction, and repeat the photocatalytic degradation experiment under the same conditions. 15 ml isopropyl alcohol (IPA), 0.15 mM p-benzoquinone (BQ) and 15 ml ethanol (EA) were added to capture ·OH, $·O^{2-}$ and H^+, respectively.

3 Results and discussion

3.1 Structure and morphology characterization

Figure 1 shows the typical XRD patterns of pure CdS and CdS/rGO nanomaterials are at 2θ = 24.8°, 26.5°, 28.18°, 36.62°, 43.68°, 47.84° and 51.82°, which exactly indexed to the (100), (002), (101), (102), (110), (103) and (112) crystal planes of the hexagonal structure conform to the CdS standard spectrum JCPDS (No. 41–1049), respectively. In addition, the diffraction peak of the CdS (101) plane is stronger than any other peaks, which indicates that the as-prepared pure CdS possess good crystallization and grows along the crystal surface (101) Compared with pure CdS, as the number of rGO increases, the peak shape of CdS/rGO nanocomposites does not change significantly, and the peak intensity gradually decreases. the evident typical carbon diffraction peaks cannot be observed due to the low amount of rGO and beyond the detection range of the instrument. For pure CdS, GCS-0.5, GCS-1.0, GCS-1.5 and GCS-2.5 nanocomposites, the crystallite size are estimated by using the Debye-Scherer equation to be 60, 34, 33, 38 and 31 nm, respectively.

Figure 2a shows the emblematical HRTEM likeness of GCS-1.0, it proves self-evident that the shape of CdS mainly show regular one-dimensional nano-sized clubbed rod structure with smooth surface and irregular clear edge, the width of the nanorod structure is basically distributed in the extent of 40–80 nm,

and the length is distributed between 100 and 300 nm, and the aspect ratio of nano-rod is very small. One-dimensional CdS nano-sized rod structure partially wrapped by graphene and partially embedded on the graphene surface, which are beneficial to transfer light carrier and improve photocatalytic activity. Figure 2b is the locally amplified HRTEM image of GCS-1.0 sample, which showing clear lattice fringe without defect structure. The statistical measurement reveal that the interplanar spacing of about 0.316 nm can be attributed to the (101) plane of the hexagonal structure of CdS. Which indicating that CdS nanocrystals grow selectively along the (101) crystal planes.

Figure 3 shows the XEDS spectra of GCS-1.0 nanocomposites. It can be seen GCS-1.0 nanocomposites only contain S, Cd and C elements characteristic peaks. The atomic and weight percentage of the related elements for GCS-1.0 nanocomposites are found to be almost close to the nominal stoichiometry used in their respective precursors, without any impurity elements from the reactants.

XPS analysis was performed to study the surface elemental composition and element electronic states. The survey spectrum of GCS-1.0 nanocomposites depict the photoemission signatures of C 1 s, Cd 3d and S 2p, as described in Fig. 4a. C 1 s spectrum can be deconvoluted into three characteristic peaks at 284.8, 286.2 and 287.7 eV as shown in Fig. 4b, assigned to C-O, C-O and C = C/C–C bonds of rGO, respectively

Fig. 1 XRD patterns of pure CdS and CdS/rGO nanocomposites
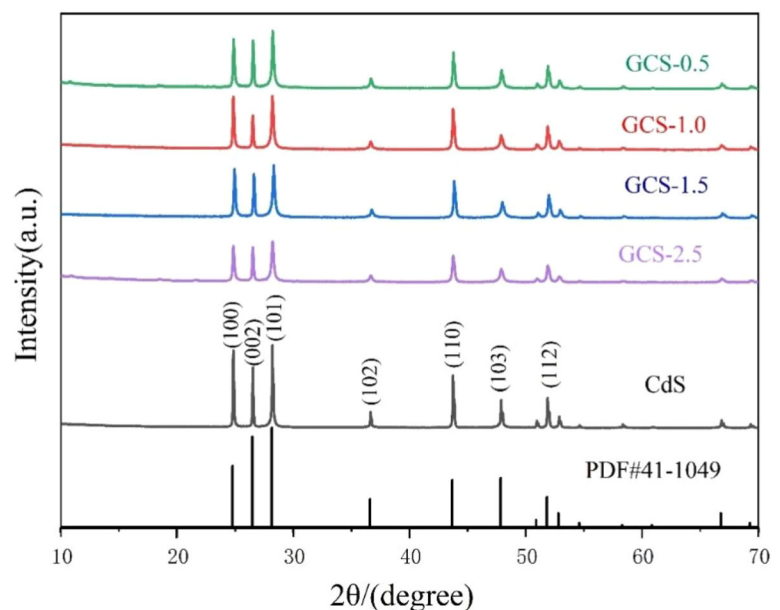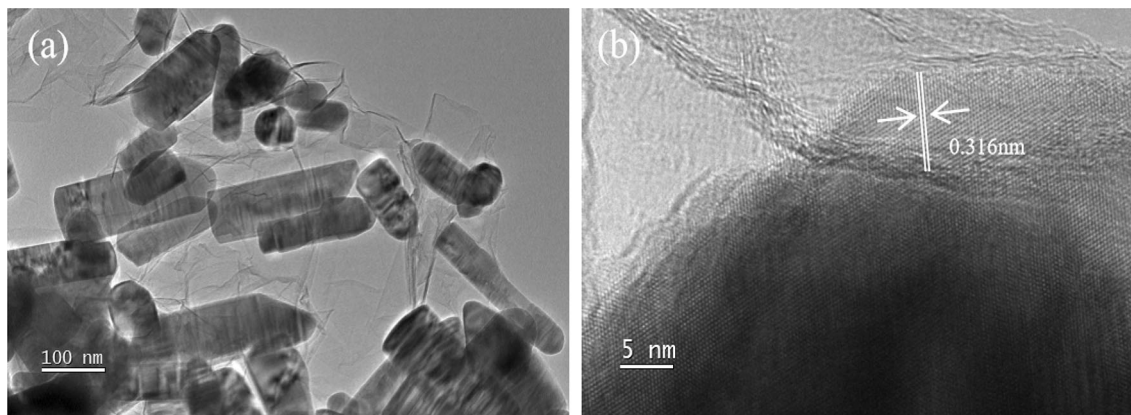
Fig. 2 a-b HRTEM images of GCS-1.0 samples

| Element	Wt%	At%
CK	14.89	50.64
SK	20.22	25.76
CdL	64.9	23.59
Matrix	Correcti	ZAF
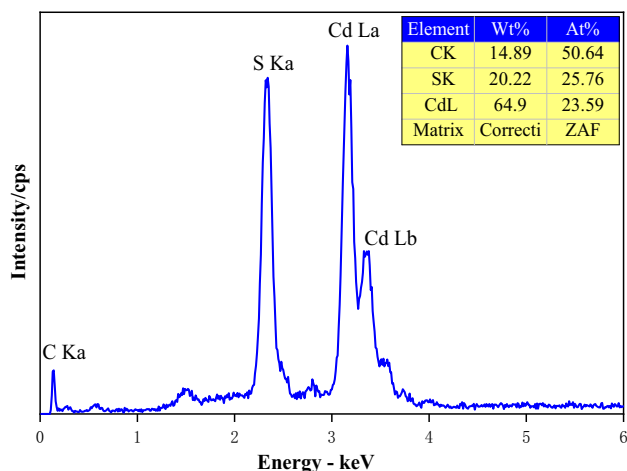
Fig. 3 XEDS spectra of GCS-1.0 samples

[35]. Figure 4c shows Cd 3d two characteristic peaks at 404.9 and 411.7 eV, which corresponding to the electron binding energies of Cd $3d_{5/2}$ and Cd $3d_{3/2}$, respectively, indicating that Cd exists in the form of Cd^{2+} state [36]. In addition, Fig. 2c displays the S2p characteristic peaks, which can be fitted into two peaks at 161.3 and 162.4 eV, belong to S $2p_{3/2}$ and S $2p_{1/2}$, respectively. Indicating that S exists in the form of S^{2-} [37] and the existence of CdS in the composite.

Figure 5 presents the typical nitrogen adsorption-desorptions isotherms and the corresponding pore size distribution curves (inset of Fig. 5) of pure CdS and GCS-1.0. It can be seen that the isotherms are relatively flat in the low-pressure region ($P/P_0 < 0.8$), the adsorption–desorption is almost overlapped due to the adsorption mainly occurs, while the isotherm increases rapidly in the high-pressure region ($P/P_0 > 0.8$) and form H_3 type

hysteresis loop owing to capillary agglomeration phenomena, indicating that the isotherms exhibit type IV and the catalysts are characteristic of mesoporous (2–50 nm) structures [25]. The average pore diameter of pure CdS is 41.67 nm with a narrow pore size distribution. The BET surface area is 16 0.88 m^2g^{-1}. Compared with pure CdS, CdS/rGO nanocomposites exhibit similar N_2 sorption characteristic, but the specific surface area and average pore diameter for GCS-1.0 is about 57.24 $m^2 g^{-1}$ and 28.36 nm, respectively. It is easy to find that the specific surface area of GCS-1.0 is more larger than that of the pure CdS sample. The pore size of the catalyst is significantly reduced after the composite, which is mainly due to the coexisting graphene nanosheet structure and well-dispersed nanorods. The larger specific surface area of the composite has more active sites conducive to the adsorption of pollutants and improves the photocatalytic deactivation of organic dyes.

Figure 6a depicts the UV–Vis absorption spectrum of pure CdS and CdS/rGO nanocomposites. From Fig. 6a, it is clear all samples display have absorption in the visible light region, it is worth mentioning that the light absorption of CdS/rGO nanocomposites obviously enhanced and exhibit better light response in the region of 550–800 nm than pure CdS. The absorbance of CdS/rGO nanocomposites increases in pace with the increase of rGO content from 0 to 2.5%, and absorption edge redshift, which may be due to the chemical bonding between CdS and rGO and the charge delimitation between CdS and rGO [33, 34].
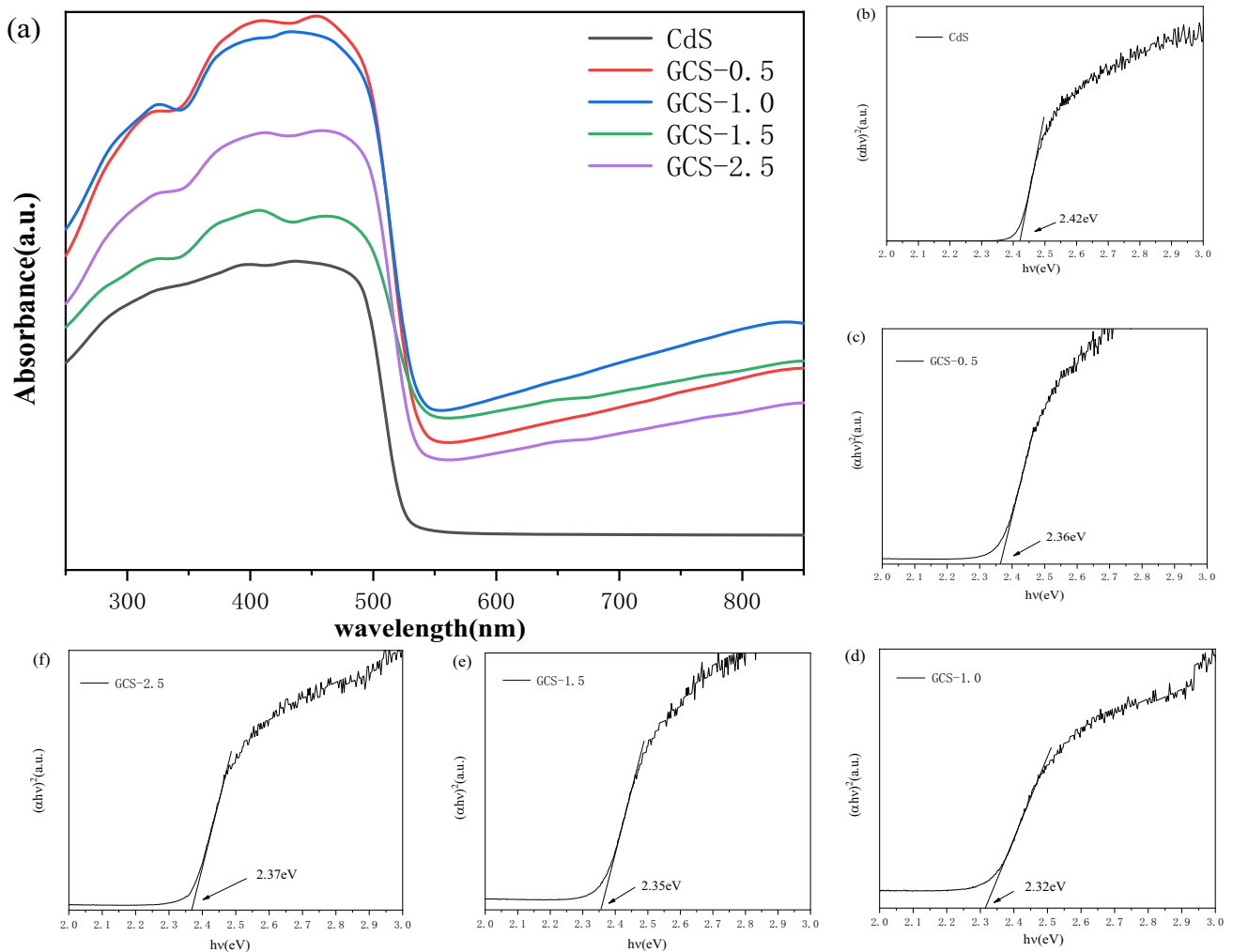
The optical band gap (Eg) of CdS/rGO nanocomposites are calculated by using the Kubelka–Munk
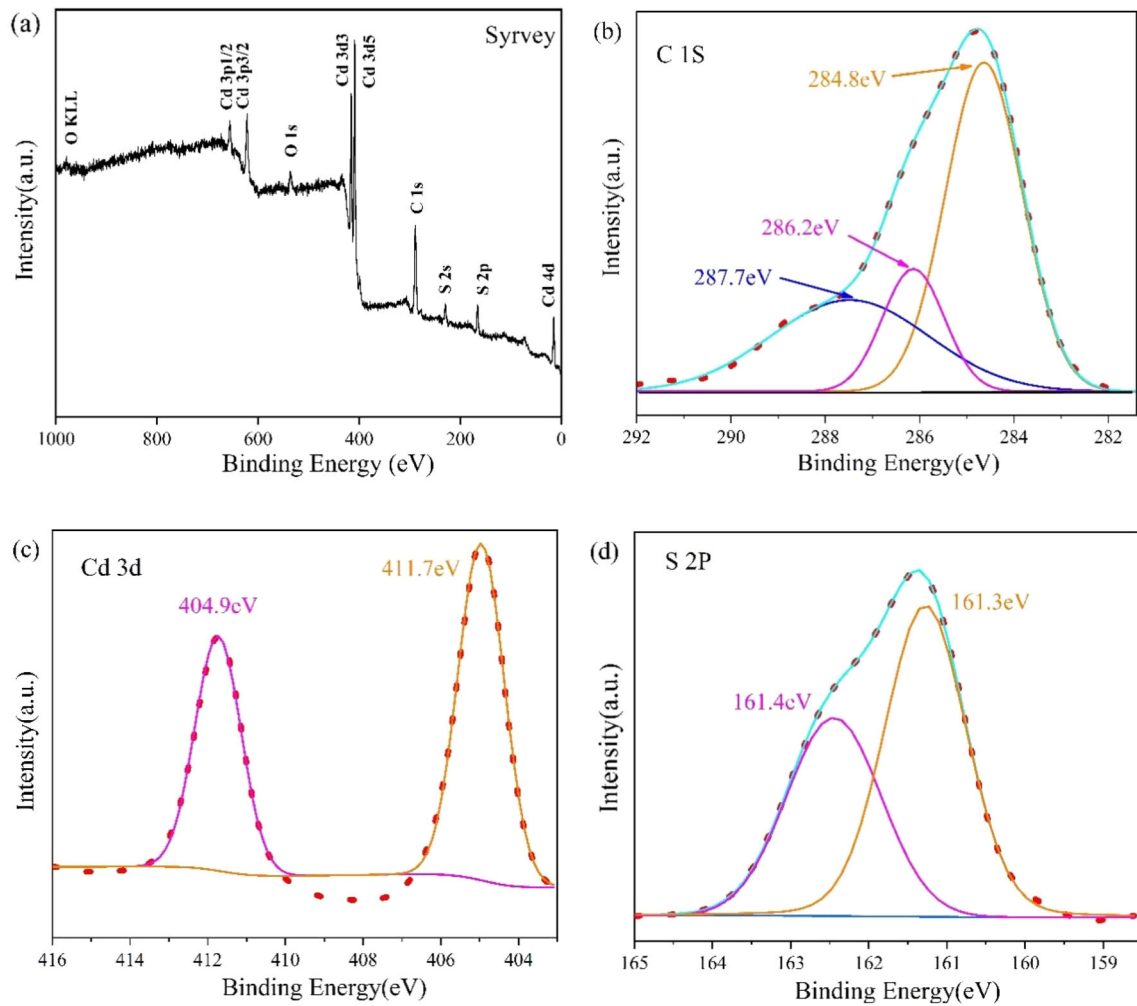
Fig. 4 XPS spectrometer of CGS-1.0 composites **a** survey spectrum, **b** C 1 s, **c** Cd 3d and **d** S 2p
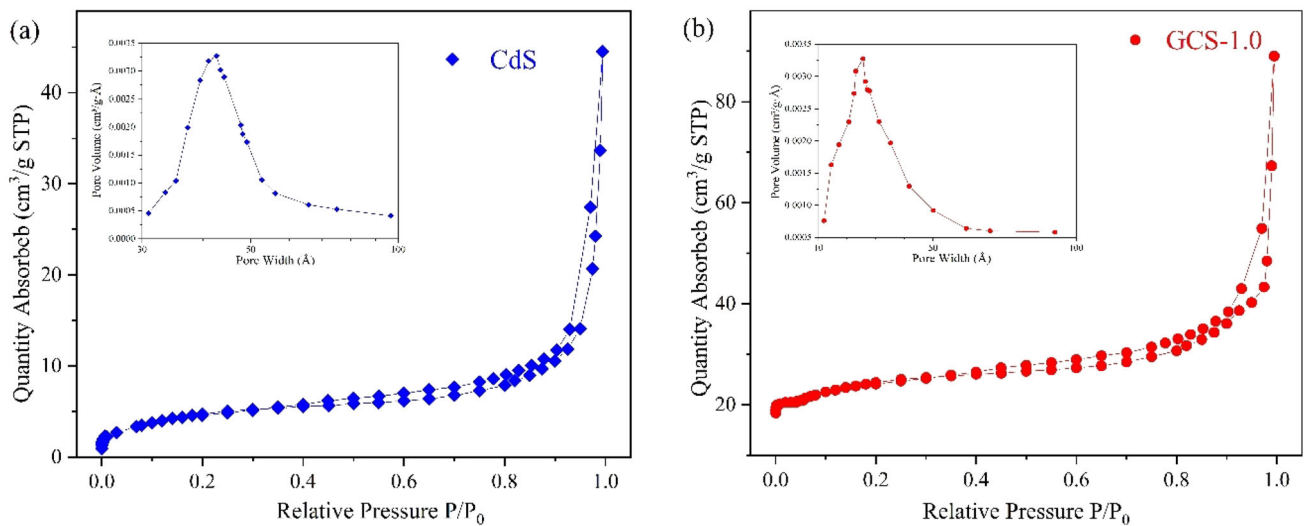
Fig. 5 Nitrogen adsorption–desorption isotherms and the corresponding pore size distribution curves of pure CdS and GCS-1.0

Fig. 6 **a** UV–vis absorption spectra and **b**–**f** the $(\alpha h\nu)^2$ versus $h\nu$ curve of pure CdS and CdS/rGO samples

relation [32], as displayed in Fig. 6b–f, the band gap energy of pure CdS, GCS-0.5, GCS-1.0, GCS-1.5 and GCS-2.5 are calculated to be 2.42, 2.36, 2.32, 2.35 and 2.37 eV, separately. The band gap of CdS/rGO nanocomposites is significantly smaller than that of pure CdS, with the increase of GO content, the band gap decreases and occurs red shift. This result probably attributed to the fact that CdS nanoparticles are enclosed in graphene and confined in a small space. The surface effects of nanocrystals cause electronic transitions towards the long wave direction.

3.2 Optical and photo-electrochemical properties analysis

Figure 7 shows the PL spectra of pure CdS and CdS/rGO nanocomposites. It is obviously that all samples exhibit two luminescence centers at 550 nm and

580 nm, respectively, the peak located at 550 nm of CdS/rGO nanocomposites decreased clearly contrast to pure CdS, and the luminescence intensity of GCS-1.0 is the weakest, which reflecting the recombination efficiency of photogenerated e^- and h^+ is low. The peak centered at 550 nm may be related to the emission from structural defects. The peak centered at 580 nm may be due to the holes in the CdS valence band recombine with electrons trapped in sulfur vacancies. Figure 7 shows that pure CdS shows the strongest PL emission signal and the shortest lifetime of carriers due to the high recombination of photogenic carriers. The PL intensity of CdS/rGO nanocomposites is significantly reduced and the carrier lifetime is obviously extended, indicating that CdS nanoparticles are modified on the surface of two-dimensional layered rGO nanostructure can
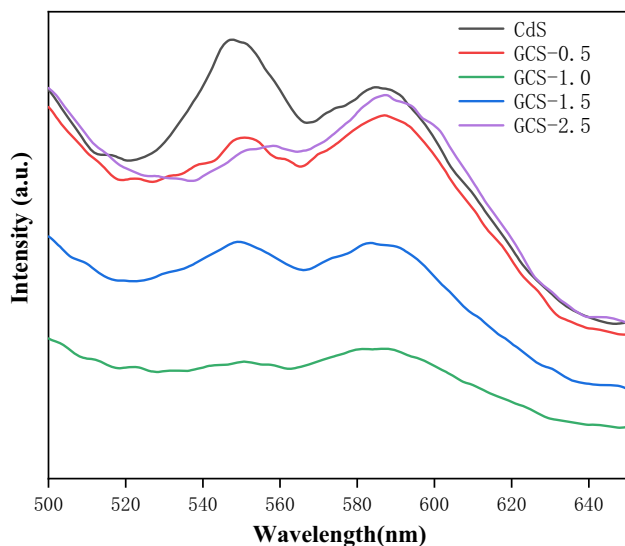
Fig. 7 PL spectra of pure CdS and CdS/rGO samples

effectively suppress the recombination of photogenic carriers, and improve the quantum efficiency of CdS/rGO nanoparticles, which is beneficial to the amelioration of photocatalytic reaction.

For the sake of further discuss the effects of the rGO mass ratio on the photo-electrochemical properties, the generation, separation and migration ability of photogenic carriers were carried out for CdS/rGO nanocomposite material. In the Fig. 8a, EIS Nyquist plots of pure CdS and CdS/rGO electrodes and the inset show the high frequency region of the spectrum expands. Obviously, the Nyquist diagram of the sample is composed of an approximate similar straight line in the low frequency area and the approximate semicircle in the high frequency area. The diameter of the arc of CdS/rGO nanocomposites smaller than pure CdS, indicating that the nanocomposites possess lower charge transfer resistance due to the higher electronic conductivity of rGO and the synergism between rGO and CdS, therefore, the catalysts can significantly improve the transfer productiveness of photo-generated carriers.

The transient photocurrent response of pure CdS and CdS/rGO nanocomposites for five on/off cycles were performed under simulated solar radiationas shown in Fig. 8b. Under the visible light raying, the photocurrent density of pure CdS, GCS-0.5, GCS-1.0, GCS-1.5 and GCS-2.5 rapidly increased to 0.0004, 0.0006, 0.11, 0.045, 0.014 mA cm^{-2}, respectively, while the light is turned off, the photocurrent drops rapidly to zero. Compared with pure CdS, the light

current density of CdS/rGO nanocomposites is significantly improved, and the photocurrent density increases with the amount of rGO compound increases. The I-t curves of CdS/rGO nanocomposites are highly accordant with the results of PL spectroscopy. The enhanced photocurrent density and weakened PL intensity of CdS/rGO nanocomposites indicates that rGO nanostructure can validly restrain the recombination of photo-generated carriers and enhance electron transfer ability in the photocatalytic reactions. GCS-1.0 exhibits the largest photocurrent density, which is most conducive to the improvement of photocatalytic performance.

Mott-Schottky analysis of CdS/rGO nanocomposites under different frequencies in 0.1 M Na$_2$SO$_4$ aqueous solutions were used for evaluate the flatband potential position and the intrinsic carrier density of photocatalyst, as shown in Fig. 9a–e. According to the formula: $N_d = \left(\frac{2}{\varepsilon_0 e_0 \varepsilon_r}\right)\left[d\left(1/C^2\right)/dV\right]^{-1}$ [38] calculate the carrier density, where ε_r is the relative dielectric constant, ε_0 is the vacuity dielectric constant, e_0 is the electron charge, N_d is the carrier denseness, C is the space charge capacitance. From Fig. 9a–e we can know that all samples exhibit n-type semiconductors characteristics due to the positive slope in the linear region of the Mott − Schottky plots [39]. According to V(NHE) = V(SCE) + 0.059pH + 0.242(pH = 7), the relative standard calomel electrode (vs SCE) potential is converted to the standard hydrogen electrode (vs NHE) potential. It can be seen from Fig. 9a that V(SCE) = − 1.115 V. Since CdS is an n-type semiconductor, the conduction band potential of CdS is VCB = V(NHE) = − 0.51 V. According to UV–Vis absorption spectrum analysis, the band gap of pure CdS is 2.42 eV, and the corresponding valence band is deduced to be 1.91 eV. The carrier densities of pure CdS, GCS-0.5, GCS-1.0, GCS-1.5 and GCS-2.5 are 6.11×10^{18}, 6.21×10^{18}, 4.47×10^{19}, 2.11×10^{19}, 1.49×10^{19} cm^{-3}, respectively. It can be seen the carrier density of CdS/rGO nanocomposites is greater than that of pure CdS, and the carrier density increases with the increase of the GO composite content.
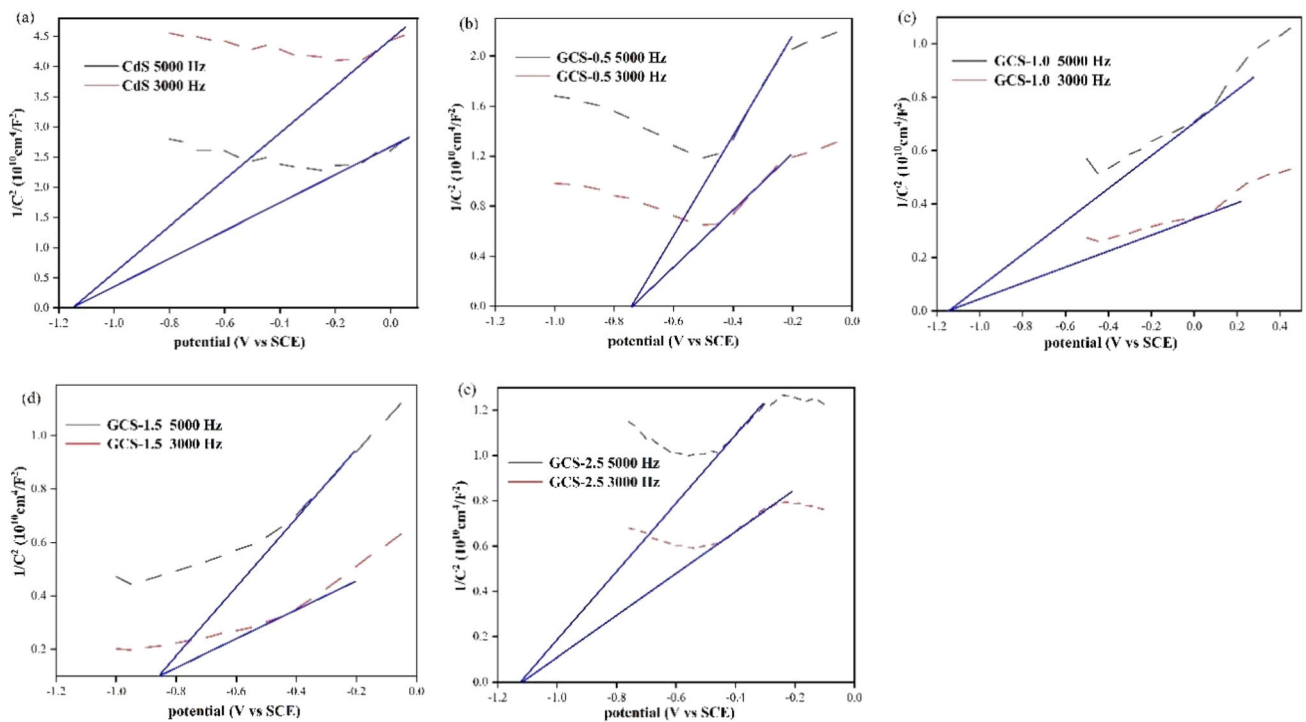
3.3 Photocatalytic activity

As can be seen in Fig. 10a the degradation rates of MO for pure CdS and CdS/rGO composite material.
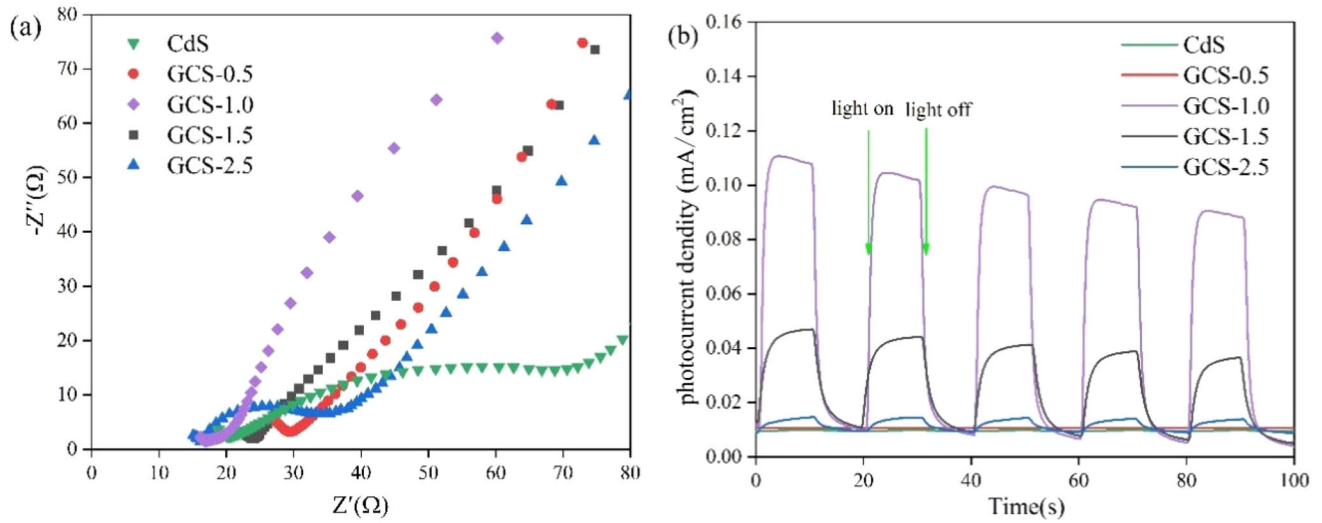
**Fig. 8 a** EIS Nyquist plots and **b** transient photocurrent responses of pure CdS and CdS/rGO samples

Fig. 9 Mott–Schottky plots for the **a** CdS and **b**–**e** CdS/rGO samples

In the blank experiment without photocatalyst, the self-degradation of MO can be disregard, which indicates that MO shows good stability. Under the combined action of simulated solar irradiation and catalyst, the degradation rate of pure CdS, GCS-0.5, GCS-1.0, GCS-1.5 and GCS-2.5 are: 21.6%, 33.4%, 85.6%, 55.2% and 43.8%, respectively. Apparently, the photocatalytic efficiency of CdS/rGO nanocomposites is superior to that of pure CdS and GCS-1.0 display the highest photocatalytic activity within 120 min, which is 4 times that of pure samples.

The plots of $Ln(C_t/C_0)$ vs time of irradiation of the photocatalytic degradation MO for CdS/rGO nanocomposites as present in Fig. 10b. The kinetic
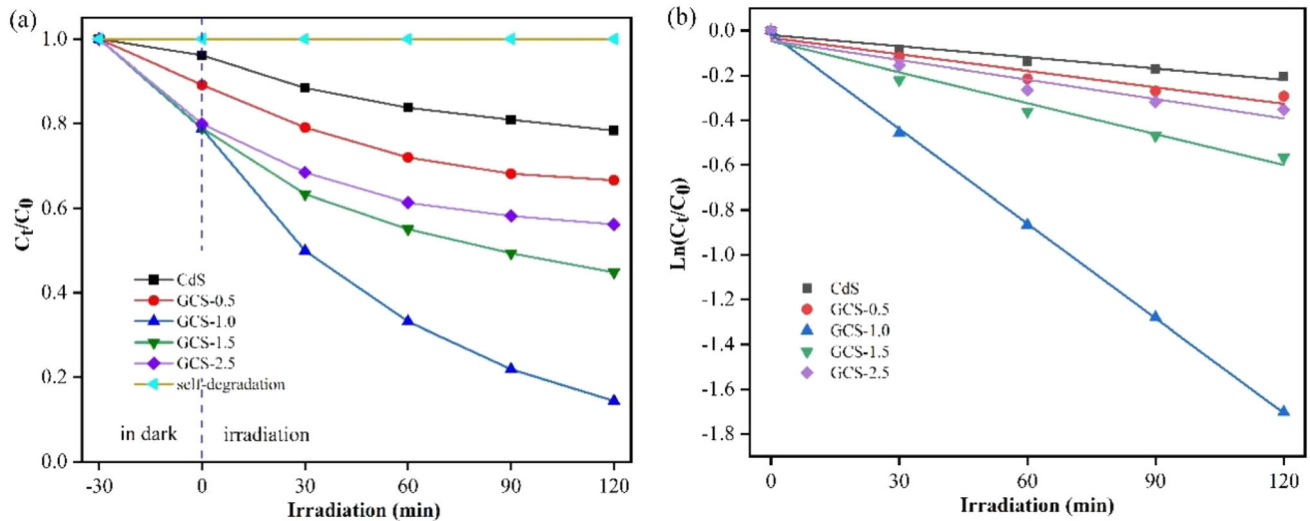
Fig. 10 a The photocatalytic degradation of MO over time and **b** plots of ln (Ct/C0) vs irradiation time for pure CdS and CdS/rGO samples

characteristics of photocatalytic degradation MO in line with first-order kinetic model equations, the rate constant for pure CdS, GCS-0.5, GCS-1.0, GCS-1.5 and GCS-2.5 samples are 0.00166, 0.00245, 0.01409, 0.00461and 0.00289 min^{-1}, respectively. It is clear the rate constant of CdS/rGO nanocomposites is greater than that of pure CdS, and GCS-1.0 display the highest photocatalytic activity within 120 min, which is 8.5 times that of pure samples. GCS-1.0 sample exhibits the largest rate constant, indicating that GCS-1.0 has the optimal photocatalytic performance.

To evaluate the stability and repeatability of photocatalytic degradation of MO for CdS/rGO nanocomposites, the cyclical stability and durability of GCS-1.0 photocatalysts were carried out for 5 successive cycles under the same conditions. As shown in Fig. 11a, the degradation efficiency decreases slightly as the number of cycles increases, after 5 cycles, the degradation efficiency reduced from the initial 85.6% to 77.8%. CdS/rGO photocatalysts exhibit excellent recyclability due to lead into the rGO on the surface of CdS, which protects CdS from photo-corrosion and enhances its photostability. As shown in Fig. 11b, the characteristic peak of the photocatalyst GCS still exists after the photocatalytic reaction. It was proved that the crystal structure of the composite material GCS did not change before and after photocatalysis, indicating that it has satisfactory structural stability. It also proved that GCS could effectively carry out long-term photocatalytic reactions.
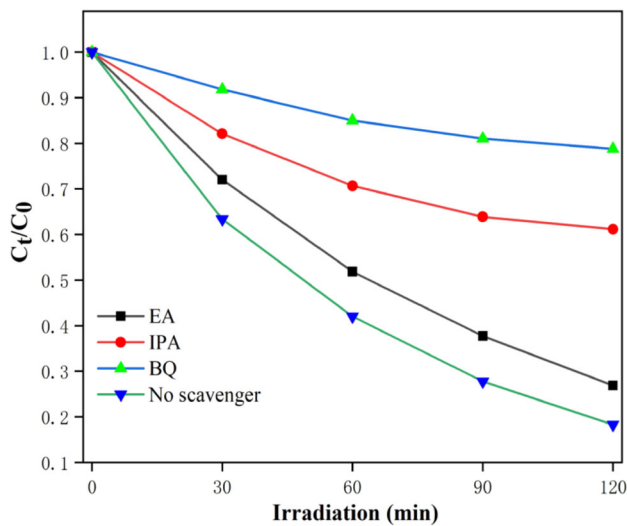
3.4 Photocatalytic mechanism

In order to grope for the contribution of reactive species on the photocatalytic degradation process of dye by adding isopropyl alcohol (IPA, used to capture hydroxyl radical ·OH), Ethanol (EA, used to capture hole h$^+$) and benzoquinone (BQ, used to capture superoxide radical ·O_2^-). Figure 12 shows the photocatalytic degradation rate of MO by GCS-1.0 photocatalysts under the presence of different capture agents. It is clear that the degradation rate reduced from the initial 81.8% to 73.1%, 38.8% and 21.2% after adding EA, IPA and BQ as scavengers, respectively. Which illustrating that ·O_2^- and ·OH play outstanding roles in the photocatalytic degradation process, while h$^+$ plays a secondary role.

Based on the above experimental results, the reasonable photocatalytic degradation mechanism of the photocatalyst under simulated visible light irradiation is proposed as follows. The bandgap of CdS is 2.42 eV, and the conduction band (CB) potential and valence band (VB)potential are -0.52 and 1.90 eV, respectively. Under visible light irradiation, electrons (e$^-$) of CdS semiconductor are excited from VB to CB and generate holes(h$^+$) in VB.

Based on the above analysis, the photocatalytic mechanism of the degradation of MO by CdS/rGO is proposed (Fig. 13). With the introduction of rGO, this new nanostructure can significantly reduce the probability of charge recombination and extend the lifetime of photogenic electron hole pairs due to the
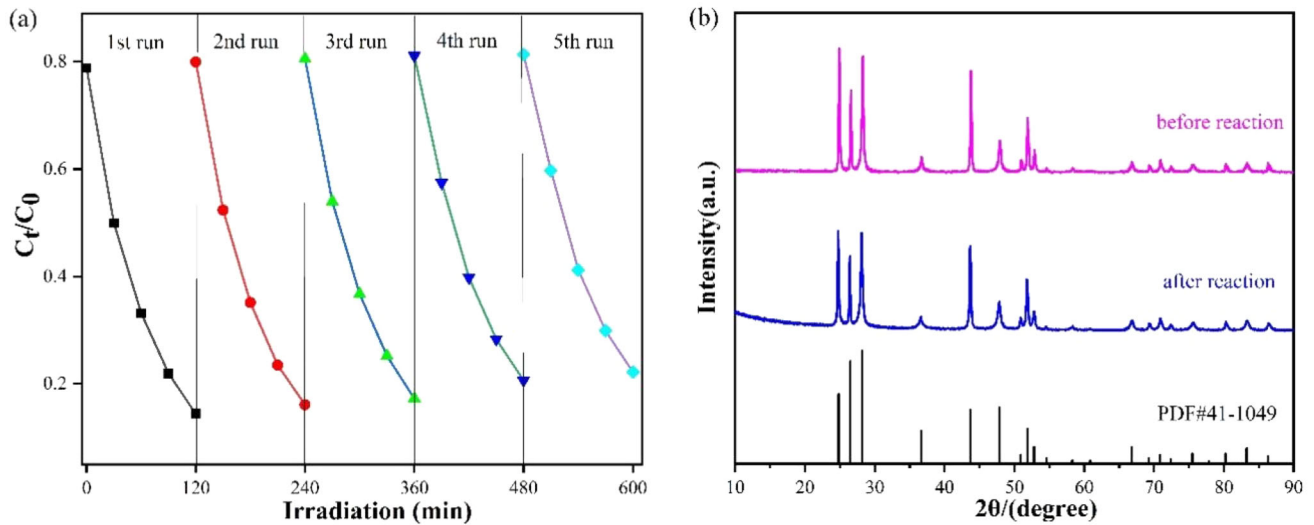
Fig. 11 **a** Recyclability of GCS-1.0 samples for photocatalytic degradation of MO and **b** XRD spectra of GCS-1.0 before and after recycling

Fig. 12 Effects of EA, IPA and BQ on the photocatalytic degradation of MO over GCS-1.0 composites
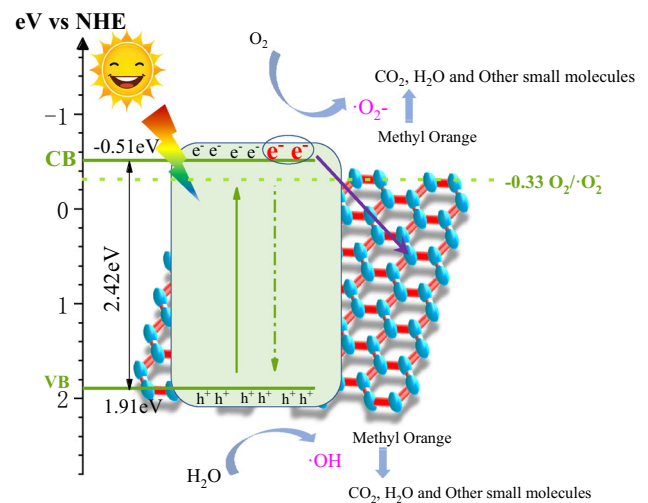
Fig. 13 The schematic diagram of photocatalytic mechanism of the CdS/rGO composites under simulated sunlight

chemical bonding of CdS/rGO interface and the excellent rGO's electron on account of the foregoing experimental results, the reasonable photocatalytic degradation mechanism of the photocatalyst under simulated visible light irradiation is proposed as follows. Under visible light irradiation, the electrons of the CdS semiconductor are excited from VB to CB, and holes are generated in VB. The electrons are immediately shifted to the surface of the catalyst and take part in the redox reactions. Photoelectrons can react with oxygen (O_2) to emerge superoxide free

radical($\cdot O_2^-$), while holes can react form hydroxyl radicals ($\cdot OH$) with water. Both $\cdot O_2^-$ and $\cdot OH$ have strong oxidation ability and can react with the pollutants to produce CO_2, H_2O and other inorganic small molecule materials. rGO plays a momentous effect in the process of photodegradation. On the one hand, rGO is utend to an electron carrier and transporter to receive and transfer photoelectrons generated on the surface of CdS and restrain the speedy recombination of electron holes. On the other hand,

rGO has a great ability to adsorb organic dye molecules.

4 Conclusions

CdS/rGO nanocomposites with enhanced photocatalytic activity were successfully fabricated via a facile one-step hydrothermal method by controlling the quality of the GO compound. Pure CdS and CdS/rGO nanoparticles are hexagonal structure with uniform particle size and good dispersion. One-dimensional CdS nanorods with smooth surface, partly decorated on the surface of graphene and partly wrapped in graphene.

The band gap of CdS/rGO nanocomposites is smaller than that of pure CdS and occurs red shift phenomenon. The photoluminescence spectra, transient photocurrent response and electrochemical impedance spectra of CdS/rGO indicate that indicating nanocomposites accelerate the separation and migration efficiency of photogenerated carriers, and inhibit the recombination of photogenerated carries, there by accelerating the redox reaction and improving its photocatalytic efficiency.

CdS/rGO nanocomposites display superior photocatalytic activity to degrade MO under the simulated sunlight irradiation than that of pure CdS, the degradation efficiency of GCS-1.0 photocatalysts remained at 77.8% after 5 cycles with excellent recyclability property. The active species capture tests demonstrate that $\cdot O_2^-$ and $\cdot OH$ play a crucial role in the photocatalytic degradation of MO for CdS/rGO nanocomposites.

Acknowledgements

Declarations

Conflict of interest The authors declare that they have no known competing financial interests or personal relationships that could have appeared to influence the work reported in this paper.

References

1. M. Yarahmadi, H. Maleki-Ghaleh, M.E. Mehr, Z. Dargahi, F. Rasouli, M.H. Siadati, J. Alloys Compd. **853**, e157000 (2021)
2. L. Zhang, L. Rao, P. Wang, Z. Shi, P. Wang, Applied Surface Science. **536**, e147726 (2021)
3. F. Chen, X. Jin, M. Jiao, D. Jia, Y. Cao, H. Duan, M. Long, Mater. Res. Bull. **132**, e110987 (2020)
4. W. Zhao, Z. Wei, L. Zhang, X. Wu, X. Wang, Mater. Sci. Semicond. Process. **88**, 173–180 (2018)
5. L. Ma, Z. Wei, X. Zhu, J. Liang, X. Zhang, J. Nanomater. **2019**, 4257270 (2019)
6. W. Zhao, Z. Wei, X. Zhang, M. Ding, S. Huang, Mater. Res. Bull. **124**, e110749 (2020)
7. A.N. Oliveros, J.A.I. Pimentel, M.D.G. de Luna, S. Garcia-Segura, R.R.M. Abarca, R.-A. Doong, Chem. Eng. J. **403**, e126213 (2021)
8. Y. Dai, M. Liu, J. Li, S. Yang, Y. Sun, Q. Sun, W. Wang, L. Lu, K. Zhang, J. Xu, W. Zheng, Z. Hu, Y. Yang, Y. Gao, Z. Liu, Sep. Sci. Technol. **55**, 1005–1021 (2020)
9. C.N.C. Hitam, A.A. Jalil, J. Environ. Manag. **258**, e110050 (2020)
10. M.-J. Fang, C.-W. Tsao, Y.-J. Hsu, J. Phys. D-Appl. Phys. **53**, e143001 (2020)
11. D. Madhan, M. Parthibavarman, P. Rajkumar, M. Sangeetha, J. Mater. Sci.: Mater. Electron. **26**, 6823–6830 (2015)
12. M. Parthibavarman, M. Karthik, P. Sathishkumar, R. Poonguzhali, J. Iran. Chem. Soc. **15**, 1419–2143 (2018)
13. S. Sathishkumar, M. Parthibavarman, V. Sharmila, M. Karthik, J. Mater. Sci.: Mater. Electron. **28**, 8192–8196 (2017)
14. R. Mu, Y. Ao, T. Wu, C. Wang, P. Wang, J. Alloys Compd. **812**, e151990 (2020)
15. H.S.H. Mohamed, M. Rabia, M. Shaban, S. Taha, Mater. Sci. Semicond. Process. **120**, e105307 (2020)
16. Z. Chen, C. Cheng, F. Xing, C. Huang, New J. Chem. **44**, 19083–19090 (2020)
17. M.A. Sulimov, M.N. Sarychev, M.V. Yakushev, J. Marquez-Prieto, I. Forbes, V.Y. Ivanov, P.R. Edwards, A.V. Mudryi, J. Krustok, R.W. Martin, Mater. Sci. Semicond. Process. **121**, e105301 (2021)
18. M. Amiri, N. Alizadeh, Mater. Sci. Semicond. Process **111**, e104964 (2020)
19. Y. Dong, Y. Su, Y. Hu, H. Li, W. Xie, Small **16**, 2001529 (2020)
20. R. Bairy, A. Jayarama, S.D. Kulkarni, M.S. Murari, H. Vijeth, Mater. Sci. Semicond. Process. **121**, e105400 (2021)
21. H. Yang, J. Fan, C. Zhou, Y. Wan, C.J.M.L. Jiang, Mater. Lett. **280**, e128317 (2020)

22. B. Poornaprakash, U. Chalapathi, M. Kumar, K. Subramanyam, S.V.P. Vattikuti, M.S.P. Reddy, S.-H. Park, Ceram. Int. **46**, 21728–21735 (2020)

23. F. Chen, X. Jin, M. Jiao, D. Jia, Y. Cao, H. Duan, M. Long, Mater. Res. Bull. **132**, e110987 (2020)

24. O.M. Bankole, S.E. Olaseni, M.A. Adeyemo, A.S. Ogunlaja, Zeitschrift Fur Physikalische Chemie-Inter. J. Res. Phys. Chem. Chem. Phys. **234**, 1681–1708 (2020)

25. Z. Wei, S. Huang, X. Zhang, C. Lu, Y. J. J. o. M. S. M. i. E. He. , J. Mater. Sci. Mater. Electron. **31**, 5176–5186 (2020)

26. G. Luna-Sanguino, A. Ruiz-Delgado, A. Tolosana-Moranchel, L. Pascual, S. Malato, A. Bahamonde, M. Faraldos, Sci. Total Environ. **737**, e140286 (2020)

27. B.M.F. Jones, D. Maruthamani, V. Muthuraj, J. Photochem. Photobiol. A: Chem. **400**, e112712 (2020)

28. T. Wang, D. Yue, X. Li, Y. Zhao, Appl. Catal. B: Environ. **268**, 118399 (2020)

29. S. Acharya, D.K. Padhi, K.M. Parida, Catal. Today **353**, 220–231 (2020)

30. M. Arya, M. Kaur, A. Kaur, S. Singh, P. Devi, S.K. Kansal, Opt. Mater. **107**, e110126 (2020)

31. P.V. Tuan, H.L. Trung, H. Chu, T.B. Hoang, V.T. Tan, H.T. Quỳnh, S. Nguyen, T.N. Khiem, Nanotechnology **32**, e015201 (2021)

32. H. Zhang, X. Lv, Y. Li, Y. Wang, J. Li, ACS nano. **4**, 380–386 (2010)

33. Z. Khan, T.R. Chetia, A.K. Vardhaman, D. Barpuzary, C.V. Sastri, M. Qureshi, RSC Adv. **2**, 12122–12128 (2012)

34. S. Manzoor, S. Husain, Mater. Res. Express. **5**, e05500 (2018)

35. A. Mondal, S. Maiti, S. Mahanty, A. Baran Panda, J. Mater. Chem. A. **5**, 16854–16864 (2017)

36. H. Gao, Z. Mo, R. Guo, X. Niu, Z. Li, J. Mater. Sci.: Mater. Electron. **29**, 5944–5953 (2018)

37. H. An, X. Yan, H. Li, B. Yang, J. Wei, G. Yang, ACS Applied Energy Materials. **2**, 4195–4204 (2019)

38. Y. Ye, H. Yang, X. Wang, W. J. , Mater. Sci. Semicond. Process. **82**, 14–24 (2018)

39. J. Pan, Z. Dong, B. Wang, Z. Jiang, C. Zhao, J. Wang, C. Song, Y. Zheng, C. Li, Applied Catalysis B-Environmental. **242**, 92–99 (2019)